Solution Structure of Murine Macrophage Inflammatory Protein-2[†,‡]

Weiping Shao,[§] L. Fred Jerva,[||] John West,[§] Elias Lolis,[||] and Barry I. Schweitzer*[,§]

Walt Disney Memorial Cancer Institute at Florida Hospital, 12722 Research Parkway, Orlando, Florida 32826, and Department of Pharmacology, Yale University School of Medicine, New Haven, Connecticut 06510

Received January 15, 1998; Revised Manuscript Received March 20, 1998

ABSTRACT: The solution structure of murine macrophage inflammatory protein-2 (MIP-2), a heparin-binding chemokine that is secreted in response to inflammatory stimuli, has been determined using two-dimensional homonuclear and heteronuclear NMR spectroscopy. Structure calculations were carried out by means of torsion-angle molecular dynamics using the program X-PLOR. The structure is based on a total of 2390 experimental restraints, comprising 2246 NOE-derived distance restraints, 44 distance restraints for 22 hydrogen bonds, and 100 torsion angle restraints. The structure is well-defined, with the backbone (N, C^{α}, C) and heavy atom atomic rms distribution about the mean coordinates for residues 9−69 of the dimer being 0.57 ± 0.16 Å and 0.96 ± 0.12 Å, respectively. The N- and C-terminal residues (1−8 and 70−73, respectively) are disordered. The overall structure of the MIP-2 dimer is similar to that reported previously for the NMR structures of MGSA and IL-8 and consists of a six-stranded antiparallel β-sheet (residue 25−29, 39−44, and 48−52) packed against two C-terminal antiparallel α-helices. A best fit superposition of the NMR structure of MIP-2 on the structures of MGSA, NAP-2, and the NMR and X-ray structures of IL-8 are 1.11, 1.02, 1.27, and 1.19 Å, respectively, for the monomers, and 1.28, 1.10, 1.55, and 1.36 Å, respectively, for the dimers (IL-8 residues 7−14 and 16−67, NAP-2 residues 25−84). At the tertiary level, the main differences between the MIP-2 solution structure and the IL-8, MGSA, and NAP-2 structures involve the N-terminal loop between residues 9−23 and the loops formed by residues 30−38 and residues 53−58. At the quaternary level, the difference between MIP-2 and IL-8, MGSA, or NAP-2 results from differing interhelical angles and separations.

A superfamily of cytokines that function as mitogens, activating agents, and chemoattractants for cells involved in the inflammatory and immune response has been identified and designated the chemokine superfamily (*1*). The chemokine superfamily is currently the largest cytokine superfamily with molecular masses ranging from 6000 to 25 000 Da, but most of the polypeptides are less than 10 000 Da. The proteins in the superfamily have been separated into two large groups based upon whether the first two of four conserved cysteines are separated by an intervening amino acid (CXC or α-chemokines) or are adjacent to each other (CC or β-chemokines). The segregation of these proteins into two groups has functional significance. In general, α-chemokines are involved in the recruitment and activation of neutrophils but not monocytes. The β-chemokines are involved in the recruitment and activation of monocytes, T cells, basophils, and eosinophils, but not neutrophils. Amino acid sequence identities between proteins within a family range from 20 to 75%, while identities across families are lower. The exceptions to the above classification include lymphotactin, which contains only two cysteines (a single disulfide) and is a chemoattractant for lymphocytes but not monocytes (*2*), and neurotactin, a membrane protein with a unique cysteine pattern (*3*).

Macrophage inflammatory protein-2 (MIP-2),[1] an α-chemokine, was first characterized as an 8 kDa, heparin-binding protein secreted from LPS-activated macrophages (*4*, *5*). Along with MIP-1α and MIP-1β, these proteins are among the most abundant proteins secreted after LPS stimulation of macrophages, constituting about 2.5% of the proteins in the conditioned medium. Intradermal injection of MIP-2 elicits a marked inflammatory response characterized predominantly by neutrophil infiltration (*4*, *5*). Animal models of glomerulonephritis (*6*), arthritis (*7*), pulmonary inflammation (*8*), and sepsis (*9*) indicate that MIP-2 is involved in the pathophysiology of these conditions. Anti-MIP-2 antibodies limit tissue damage and, in the case of sepsis and pulmonary inflammation, provide partial protection against death. Deletion of the MIP-2 receptor from mice confirms that MIP-2 is essential for neutrophil chemotaxis and provides evidence that MIP-2 is involved in hematopoiesis (*10*). In vitro studies are also consistent with a role for MIP-2 in hematopoiesis as MIP-2 possesses growth factor

[†] This work was supported in part by a research grant from the Arthritis Foundation to E.L.

[‡] Coordinates have been deposited in the Brookhaven Protein Data Bank under accession code 1mi2.pdb.

* To whom correspondence should be addressed.

[§] Walt Disney Memorial Cancer Institute at Florida Hospital.

[||] Department of Pharmacology.

[1] Abbreviations: DQF-COSY, double quantum filtered correlation spectroscopy; GCP, granulocyte chemotactic protein; HSQC, heteronuclear single quantum coherence; IL-8, interleukin-8; MCP, monocyte chemoattractant protein; MGSA, melanoma growth stimulatory activity; MIP, macrophage inflammatory protein; NAP, neutrophil-activating peptide; NMR, nuclear magnetic resonance; NOE, nuclear Overhauser effect; PF4, platelet factor 4; RANTES, regulated upon activation, normal T-cell expressed and presumably secreted; RMS, root-mean-square; ROESY, rotating frame Overhauser effect spectroscopy; TOCSY, total correlation spectroscopy.

S0006-2960(98)00112-3 CCC: $15.00
Published on Web 05/23/1998

activities on a number of progenitor cells in the bone marrow (*11*−*14*).

Two human seven transmembrane G protein-coupled IL-8 receptors with 77% amino acid identity have been identified (*15*, *16*) and designated CXCR1 and CXCR2. Both of these receptors are activated by and bind IL-8 and GCP-2 with high affinity (*17*), but the murine chemokines MIP-2 (*18*) and KC (*19*) and human chemokines MGSA/gro-α, NAP-2, and ENA-78 (*20*−*22*) exhibit high-affinity binding only to the CXCR2 receptor. Experiments to directly study interactions between chemokines and their receptors are difficult due to the inability to purify large amounts of soluble G protein-coupled receptors. A number of investigations have therefore focused on defining the ligand-binding sites of chemokine receptors and on defining the receptor-binding sites of chemokines.

The three-dimensional structures of PF-4 [human (*23*) and bovine (*24*)], IL-8 (*25*, *26*), MGSA [human (*27*−*29*) and rat [CINC/GRO] (*30*)], NAP-2 (*31*), MIP-1β (*32*), RANTES (*33*, *34*), MCP-1 (*35*), MCP-3 (*36*, *37*), and SDF-1α (*38*) have been determined using NMR spectroscopy or X-ray crystallography. In all cases, the secondary structure of the monomer consists of an extended N-terminus, three strands of antiparallel β-sheet folded in a Greek key, and a carboxy-terminal α-helix (reviewed in ref *39*). The subunit structures of these proteins show great variability. PF-4 and NAP-2 are tetramers (a dimer of dimers) and all of the others exist as dimers. For members of the α-chemokine family (MGSA, IL-8, NAP-2, and PF-4), the two monomers associate to form an extended six-stranded β-sheet with most of the subunit−subunit interactions formed between the first β-strand of each monomer. The tetramers of NAP-2 and PF-4 are formed by back-to-back association of the extended β-sheets of the two dimers. The solution structures of proteins from the β-chemokine family show an entirely different quaternary architecture. The dimer interface of MIP-1β, RANTES, and MCP-1 is formed by a completely different set of residues located predominantly at the extended loop of the amino terminus. This interface gives rise to an elongated, cylindrical molecule in contrast to the globular molecule of α-chemokines. Fully active monomeric chemokines have been also observed (*40*), but the nature of the quaternary structure of chemokines bound to receptors has not been characterized.

Murine MIP-2 shares about 40% amino acid sequence identity with IL-8; therefore, it is not surprising that the two proteins bind the same receptor (CXCR2) and exhibit similarities in their function. Nevertheless, significant dissimilarities are also evident, suggesting that some structural difference exists between the two chemokines. As part of the effort to clarify the origin of the different binding specificities and activities of these chemokines to their receptors, we have determined a solution structure of murine MIP-2 at high resolution by using two-dimensional homonuclear and heteronuclear NMR spectroscopy and torsion angle molecular dynamics calculations.

MATERIALS AND METHODS

Sample Preparation. Recombinant MIP-2 was produced in the *Pichia pastoris* expression system as previously described (*18*). Two hundred milliliters of buffered glycerol-complex media (BMGY) contained 1% yeast extract, 2% peptone, 100 mM potassium phosphate, pH 6.0, 1.34% yeast nitrogen base (without amino acids), 1.6 μM biotin, and 1% glycerol was used for *P. Pastoris* growth. After 48 h of growth at 30 °C with vigorous shaking, the culture was pelleted by centrifugation and resuspended in 200 mL of buffered methanol-complex media in which the 1% glycerol in BMGY is replaced by 1% methanol to initiate induction. Methanol was resupplied every 24 h to a final concentration of 1%. After 72 h, the culture was pelleted at 10 000 rpm and the supernatant was decanted and passed over a 0.2 μm filter prior to loading onto a Sepharose 6B heparin affinity column (Pharmacia) equilibrated with 20 mM Tris, pH 7.4, 20 mM NaCl, and 1 mM EDTA. MIP-2 was eluted with a 0.02 to 2.0 M linear NaCl gradient and was >98% pure as judged by SDS−PAGE. MIP-2 produced in this manner has been shown by amino acid analysis to have the amino acid composition of the native protein and to have a molecular mass of 7845 Da by mass spectrometry. This is in exact agreement with the predicted molecular mass based on the amino acid sequence and the loss of four hydrogen atoms upon formation of two disulfide bonds (*18*).

NMR samples were prepared by dialyzing the purified protein against 0.1 M ammonium acetate, lyophilizing the protein, and dissolving the lyophilized protein in 90% H_2O/10% D_2O or D_2O. The pH was adjusted to pH 5.25 by adding microliter increments of DCl or NaOD to a 0.6 mL sample. The final protein concentration of MIP-2 used for the detailed NMR analysis was 2 mM.

NMR Spectroscopy. All NMR experiments were carried out on a Varian UNITY Plus 600 MHz spectrometer equipped with a 5 mm PFG triple-resonance probe. The majority of NMR spectra were recorded at a temperature of 303 K; some experiments were also recorded at 298 K and 308 K to resolve ambiguities. Clean TOCSY (*41*−*43*) experiments were carried out with mixing times of 15, 30, 65, 80, and 100 ms. NOESY (*44*, *45*) experiments were carried out with mixing times of 50, 100, 150, and 200 ms. A ROESY (*46*) experiment was carried out with a mixing time of 35 ms. A DQF-COSY experiment (*47*) was also performed. All spectra were recorded in the phase-sensitive mode according to the method of States et al. (*48*), with spectral widths of 10 kHz in both dimensions. The water resonance in TOCSY and NOESY spectra was suppressed by using the WET solvent suppression technique (*49*). Twenty millisecond selective pulses with a SEDUCE (*50*) profile were employed in these experiments. In other experiments, low-power preirradiation of the water resonance was used for solvent suppression.

The spectra were processed and analyzed using Felix 95 (Molecular Simulations, Inc, San Diego, CA). Prior to Fourier transformation in t_2, the NOESY and TOCSY data were multiplied by a weak Lorentzian to Gaussian window function and zero-filled to yield final spectra of 2 K × 2 K points. DQF-COSY data were processed using a exponential weighting in t_2 and a sine-bell function in t_1 and zero-filled to 8 K × 1 K points. Additional suppression of the water signal was achieved by convolution of the time-domain data.

A 2D ^{1}H-^{15}N HSQC experiment (*51*) was acquired at natural abundance. GARP-1 was used to decouple ^{15}N during the acquisition period. The ^{1}H and ^{15}N carriers were placed at the water frequency and 119.0 ppm, respectively,

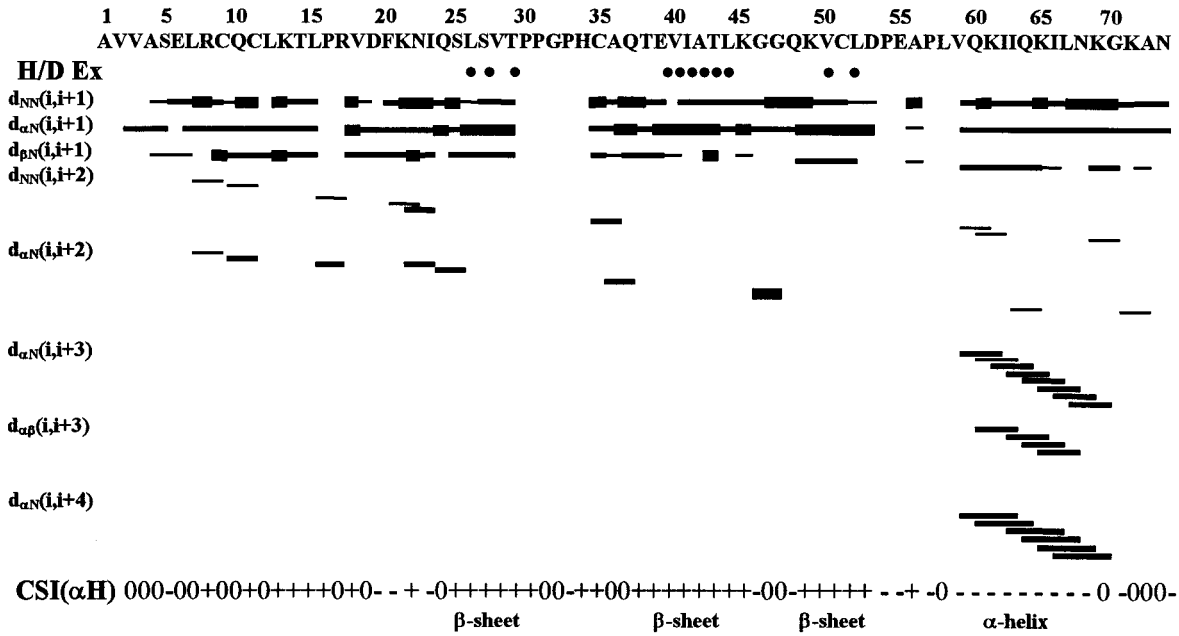

FIGURE 1: Summary of the sequential NOE connectivities, backbone amide proton exchange rates, and chemical shift index of $C^{\alpha}H$ protons for MIP-2. The relative strengths of the NOEs are indicated by the thickness of the lines. Slowly exchanging amide protons are indicated by a solid circle. The chemical shift index of each $C^{\alpha}H$ is indicated by "−", "0", or "+", corresponding to the indices −1, 0, +1, respectively, described by Wishart et al. (*66*).

with spectral widths of 10 kHz (^{1}H) and 6 kHz (^{15}N). The acquired data consisted of 96 complex data points in t_1 (^{15}N) and 2048 complex data points in t_2 (^{1}H). Zero-filling and linear prediction were employed to yield a final spectrum of 2048 (^{15}N) × 2048 (^{1}H).

Slow amide proton exchange with solvent was measured at 303 K by repeated acquisition of TOCSY spectra, acquired 0.5 h following dissolution of the lyophilized protein sample in D_2O. The total acquisition time for a TOCSY spectrum was approximately 4 h. Qualitative hydrogen exchange rates were derived by comparison of amide proton cross-peak volumes as a function of acquisition time.

Interproton Distance and Stereospecific Restraints. Interproton distance restraints were derived from NOEs assigned in the 2D NOESY spectrum acquired with a mixing time of 100 ms. The assigned NOE intensities measured by volume integration were converted into distances referenced to the long-range β-sheet NOE between $C^{\alpha}H$ and backbone NH as 3.2 Å (*52*) and were divided into four groups with distance ranges of 1.8−2.7 Å (1.8−2.9 Å for NOEs involving NH protons), 1.8−3.3 Å (1.8−3.5 Å for NOEs involving NH protons), 1.8−5.0 Å, and 1.8−6.0 Å, corresponding to strong, medium, weak, and very weak NOEs. In the case of distance restraints involving methyl protons, an additional 0.5 Å was added to the upper distance limit to account for averaging due to the rapid rotation of the methyl group (*53*, *54*). Stereospecific assignments were made by observation of intraresidue and sequential NOESY and ROESY peak intensities (*55*−*57*) and from results of initial structure calculations. If NOEs were observed from a proton to both methylene protons, which were not stereospecifically assigned, the weaker NOE was explicitly used for the restraints. Where appropriate, $\langle r^{-6}\rangle$ summation was applied to NOEs involving nonstereospecifically assigned methylene protons (*58*−*60*).

Dihedral Angle Restraints. Backbone ϕ angles were calculated from the $^3J_{HN-H\alpha}$ scalar coupling constants measured from the DQF-COSY spectrum using the method of Kim and Prestegard (*61*). Backbone ϕ angles measured in this way were only used in structural calculations for residues within elements of clearly defined secondary structure, in which case these angles were restrained to values of −60° ± 30° or −140° ± 30° for α-helix or β-sheet, respectively. For those residues in which $^3J_{HN-H\alpha}$ could not be measured, the ϕ torsion angle was restrained to −100° ± 80° if the amide proton gave a more intense NOE to the $C^{\alpha}H$ proton of the preceding residue compared with the NOE to its own $C^{\alpha}H$ proton (*62*). Side chains in which H_{α}-$H_{\beta 1}$/H_{α}-$H_{\beta 2}$ cross-peak intensity ratios were greater than 5 in short mixing time (15 ms) TOCSY experiments in D_2O were assumed to have a χ_1 angle between 120° and 360° (*33*). Side chains in which both H_{α}-H_{β} cross-peaks were weak had χ_1 restrained between 0° and 120°.

Hydrogen Bonding and Disulfide Restraints. Backbone hydrogen bonds were identified from the pattern of sequential and interstrand NOEs involving NH and $C^{\alpha}H$ protons, together with hydrogen exchange rate measurements. An amide proton with a measurable exchange rate under the experimental conditions of 303 K and pH 5.25 was considered as a possible hydrogen bond donor. Only hydrogen bonds that satisfied both NOE connectivity criteria and hydrogen exchange rates were used for structure calculations. Each hydrogen bond identified was defined using two distance restraints, d_{H-O} = 1.7−2.0 Å and d_{N-O} = 2.7−3.0 Å. One distance restraint ($d_{S\gamma i-S\gamma j}$ = 2.1 Å) was used to define the disulfide bonds between residues 9 and 35 and 11 and 51.

Structure Calculations. Structure calculations were carried out with a torsion angle molecular dynamics protocol (*63*) using the program X-PLOR 3.851 (*64*). Initial structures consisted of extended strand conformations which were generated by sequentially placing all atoms along the *x*-axis at tenth of an angstrom intervals, with *y* and *z* coordinates set to random numbers between zero and 1. In the first stage,

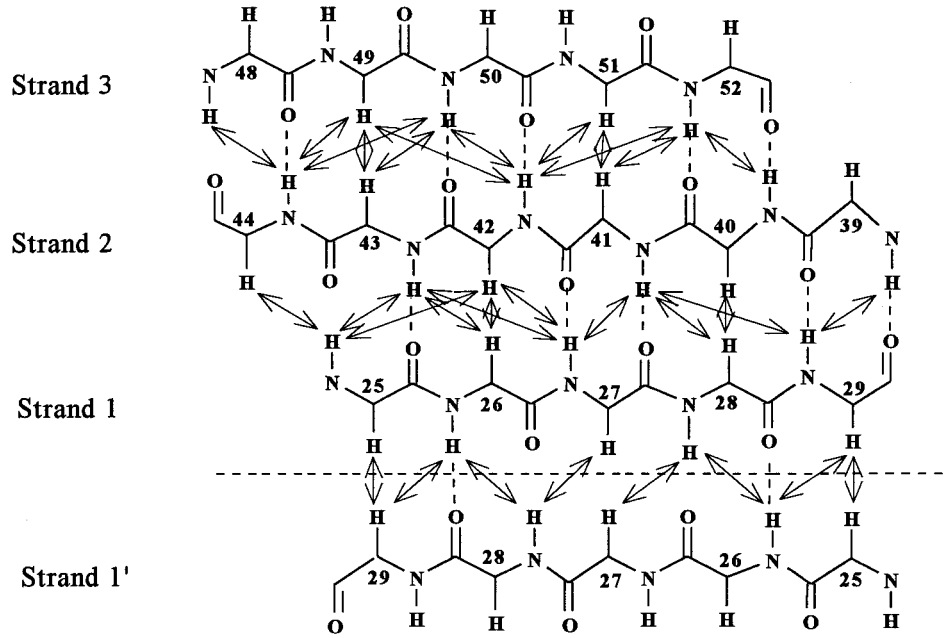

FIGURE 2: Schematic representation of the antiparallel β-sheet and dimer interface of MIP-2 as determined by analysis of NOE connectivities and amide proton exchange data. Observed interstrand NOEs are indicated by arrows. Hydrogen bonds predicted from amide proton exchange and NOE data are indicated by broken lines.

Table 1: Structural Statistics for the Ensemble of 20 Structures and Atomic Differences to the Mean Structure (Residues 9−69)

rms deviation from experimental distance restraints (Å)	
NOE (2246) + H-bond (44)	0.031 ± 0.004
dihedral restraints (deg)	
ϕ angles (80) + χ_1 angles (20)	0.359 ± 0.073
deviation from idealized covalent geometry	
bonds (Å)	0.0030 ± 0.0003
angles (deg)	0.599 ± 0.017
impropers (deg)	0.493 ± 0.020
avg rmsd from mean structure	
backbone atoms (N,Cα,C) (Å)	0.57 ± 0.16
all heavy atoms (Å)	0.96 ± 0.12

the regularized extended strands were subjected to 30 ps of torsion-angle molecular dynamics at 50 000 K. To facilitate rotational barrier crossings, the scaling factor for the van der Waal energy, $w_{vdw,}$ was set to 0.1. The structures were then subjected to a slow-cooling torsion-angle molecular dynamics stage in which the temperature was reduced from 50 000 to 1000 K over a period of 30 ps while w_{vdw} was linearly increased from 0.1 to 1.0. The NOE and dihedral force constants were held at 150 kcal mol^{-1} Å^{-2} and 100 kcal mol^{-1} rad^{-2}, respectively. The third stage of the protocol consisted of a slow-cooling stage from 1000 to 300 K for 6 ps using Cartesian molecular dynamics. During this stage of the protocol, the NOE and dihedral force constants were kept at 50 kcal mol^{-1} Å^{-2} and 300 kcal mol^{-1} rad^{-2}, respectively. Finally, the structures were subjected to 1000 steps of conjugate-gradient minimization. Symmetry restraints were applied throughout the torsion angle molecular dynamics procedure in the form of the X-PLOR noncrystallographic symmetry (NCS) restraint to ensure that the rms difference between the two monomers within a single dimer was minimized.

A total of 2246 NOE distance restraints (976 intraresidue, 608 sequential, 238 medium-range, 374 long-range, and 50 intersubunit NOEs) were used. In addition, 100 dihedral restraints (80ϕ and 20χ_1) and 44 hydrogen-bonding restraints (from 22 hydrogen bonds) were used. The stereochemical quality of the ensemble was assessed with the program PROCHECK (*65*).

RESULTS AND DISCUSSION

Resonance Assignments. The sequential assignment of the residues in the ^{1}H NMR spectrum was achieved by first identifying spin systems using TOCSY spectra acquired with different mixing times and DQF-COSY spectra. This procedure was followed by assigning identified spin systems to particular residues in the protein by the observation of sequential HN−HN, C$^\alpha$H−HN, and C$^\beta$H−HN NOEs (*52*). Ambiguities arising from degenerate chemical shifts were resolved by recording spectra at different temperatures ranging from 298 to 308 K. The side-chain NH resonances of three Asn residues and six Gln residues were not fully resolved in the ^{1}H spectra but could be resolved in a 2D ^{15}N-^{1}H HSQC spectrum (Figure 1S, Supporting Information) and linked with C$^\beta$H or C$^\gamma$H resonances by NOEs in the NOESY spectra. ^{15}N and ^{1}H chemical shifts are listed in Table 1S (Supporting Information).

Secondary Structure and Dimer Formation. The secondary structure of MIP-2 was determined from a qualitative analysis of the sequential, medium-range and some long-range backbone NOE intensities, backbone scalar coupling constants, amide proton exchange rates, and chemical shift analysis of C$^\alpha$H protons. MIP-2 contains a three-stranded antiparallel β-sheet, characterized by stretches of strong sequential [$d_{\alpha N}(i,i+1)$] NOE connectivities, long-range backbone NOE connectivities [$d_{NN}(i,j)$, $d_{\alpha N}(i,j)$, and $d_{\alpha\alpha}(i,j)$], reduced amide proton exchange rates, and the C$^\alpha$H chemical shift index of Wishart et al. (*66*) (Figure 1). The arrangement of the three β-strands into an antiparallel β-sheet is that of a Greek key: strand 2 (residues 39−44) is hydrogen bonded to strands 1 (residues 25−29) and 3 (residues 48−52), as shown in Figure 2. In addition, a C-terminal α-helix

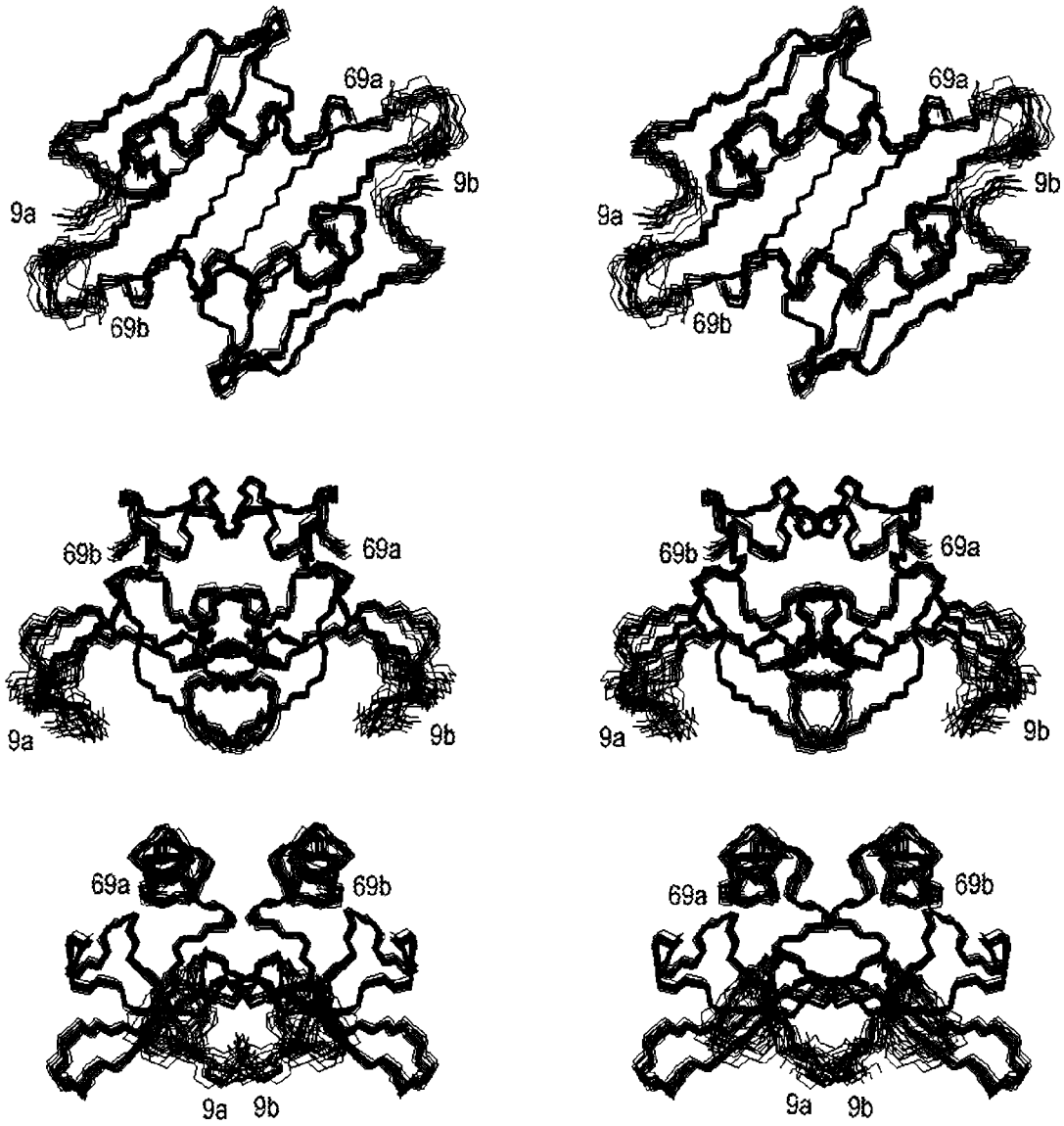

FIGURE 3: Stereoviews showing best fit superpositions of the backbone atoms of the 20 lowest energy accepted torsion angle molecular dynamics structures. Resides 9−69 from both subunits are shown in three different orientations.

extending from 60 to 67 is well-defined, as characterized by the observed grouping of $d_{NN}(i,i+1)$, $d_{NN}(i,i+2)$, $d_{\alpha N}(i,i+3)$, $d_{\alpha\beta}(i,i+3)$, and $d_{\alpha N}(i,i+4)$ NOE connectivities (Figure 1). Several medium-range NOEs involving residues 24−30, and the observation of a slowly exchanging amide proton for residue Leu-26, are consistent with MIP-2 forming a dimer in solution. Strand 1 from the β-sheet in one monomer is hydrogen bonded in an antiparallel fashion to the same strand in the other monomer (Figure 2). As mentioned above, this quaternary arrangement has been observed for other CXC chemokines, but is very different from that of the CC chemokines (reviewed in ref *39*).

Calculation of the Structure of MIP-2. Structures have been calculated for the MIP-2 dimer using distance and dihedral angle restraints generated from NMR data and a torsion angle molecular dynamics protocol (*63*). A structure calculated in this manner was considered to be acceptable if it had no violation of NOE restraints greater than 0.5 Å, no dihedral angle violation greater than 5°, no rms deviation of bonds from ideal values greater than 0.02 Å, and no rms deviation of angles from ideal values greater than 2.0°. Several rounds of calculations were performed, adding more NOEs to each round to resolve ambiguous assignments (*67*). In the final round of calculations, an average of 16 restraints per residue was used. A total of 50 structures were calculated, and 45 of these were acceptable according to the above criteria. The structural statistics of the 20 accepted structures with the lowest overall energies are shown in Table 1, and the superposition of the individual structures on the average structure is shown in Figure 3. Excluding residues 1−8 and 70−73 at the N- and C-termini of both monomers, which are poorly defined by the data, the remainder of the structure is well determined with atomic rms differences with respect to the mean coordinate positions of 0.57 ± 0.16 Å for the backbone (N, C^{α}, C) atoms and 0.96 ± 0.12 Å for all heavy atoms (Table 1).

The stereochemical quality and precision of the ensemble of 20 structures was assessed with the program PROCHECK (*65*). With regard to the ϕ/ψ locations in the Ramachandran diagram (*68*), all nonglycine residues from 9 to 69 in all 20 structures lie within the allowed region, wherein 69% of the residues were in the most favored regions, 23% were in

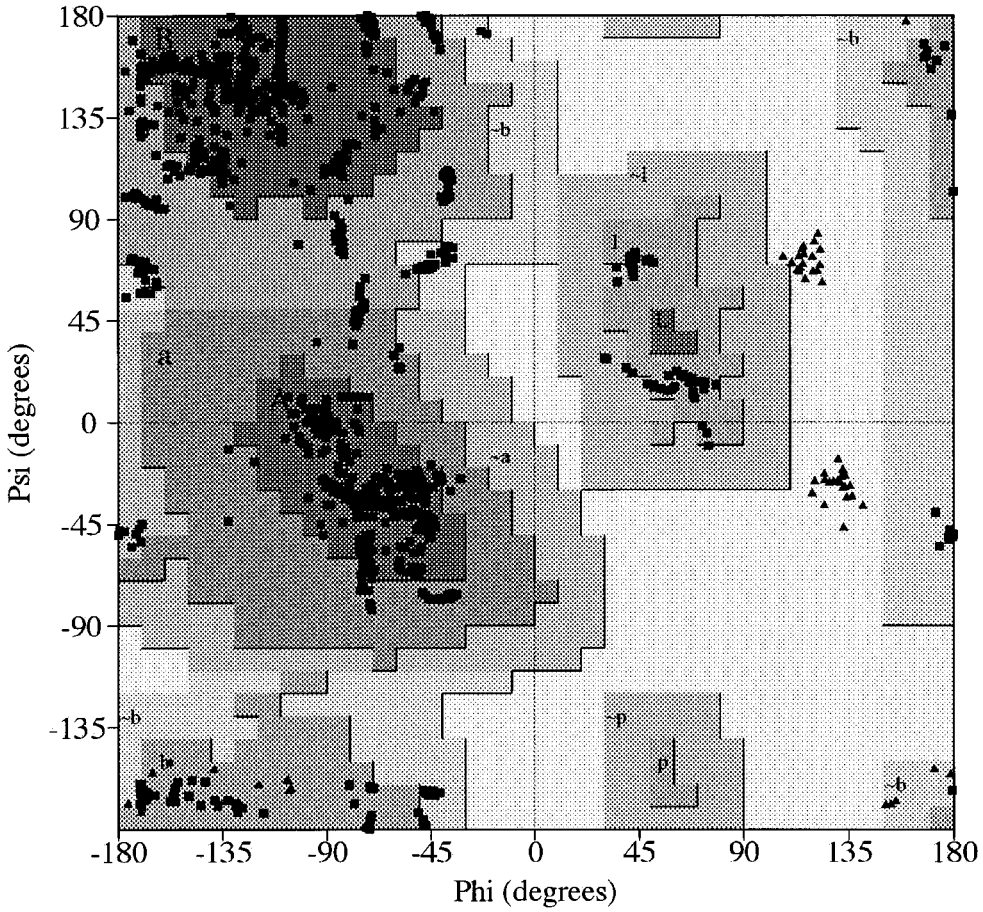

FIGURE 4: The Ramachandran plot of the distribution of $\phi-\psi$ values for residues 9−69 of 20 MIP-2 structures. The regions denoted as A, B, L are the most favored; a, b, l, and p are the additional allowed; ~a, ~b, ~l, and ~p are generously allowed. Glycine residues are shown as triangles.

additional allowed regions, and 8% were in generously allowed regions (Figure 4). The precision of the torsion angles was assessed using PROCHECK by the circular variance (*69*−*70*). The value of circular variance varies from 0 to 1, with a lower value indicating a tighter clustering of the values about a single mean value. The circular variance for the ϕ and ψ torsion angles for the majority of the residues in the structured region (residues 9−69) is low, indicating that the backbone of the structures is well-defined (Figure 4a), with the exception of residues 9−10, 32, and 35−36. This implies that these parts of the protein are either relatively more mobile or are less defined due to chemical shift degeneracy and/or lack of NOE information. Most side chains, especially the residues in the nonloop regions of the protein, are reasonably well-defined as indicated by the χ circular variance which is close to 0. Higher values of circular variance are observed for charged residues such as Lys-13, Lys-45, and Lys-61. These charged residues tend to be located on the surface of the protein as indicated by the calculated surface accessibility (Figure 4b).

Description of the Structure of MIP-2. A ribbon diagram of the overall polypeptide fold of the MIP-2 dimer is shown in Figure 6. As mentioned above, each monomer contains a three-stranded antiparallel β-sheet, arranged in a Greek key motif and packed against a C-terminal α-helix. There are four cysteines, all of which are involved in disulfide bond formation: Cys-9 forms a disulfide with Cys-35, which is part of the 30s turn, and Cys-11 forms a disulfide bond with Cys-51 of strand 3 of the β-sheet. At the N-terminus, a series of nonclassic turns at residues 9−12 and 15−18 make up a long loop extending from residues 9 to 19. This is followed by a single 3_{10}-helical turn formed by residues 20−22 that leads into strand 1. Strands 1 and 2 are connected by a loop (the 30s loop; residues 30−38) which contains no standard turns but is markedly bent between residues 34 and 35. The conformation of the β-hairpin (the 40s loop; residues 45−47) connecting strands 2 and 3 is also unusual [$\phi_{(i+1)}$ −84, $\psi_{(i+1)}$ 109; ($\phi_{(i+2)}$ 139, $\psi_{(i+2)}$ −30] and is classified as a distorted type I turn. Strand 3 of the β-sheet leads into the α-helix via a loop from residues 53 to 58 (the 50s loop). In MGSA, the α-helix extends from residue 57 to residue 69 within each subunit, while in IL-8, this α-helix continues to the C-terminal residue 73. In the case of MIP-2, residues 68−70 were found to be in a helix-like turn configuration in 9 out of the 20 torsion angle dynamics structures, and the α-helix extended from residue 60 to only 67 before fraying was observed. The secondary structure identified in MIP-2 is summarized in Figure 4c. The solvent accessibilities in Figure 4b indicate that the antiparallel β-sheet domains are either mostly buried or masked by folding of the C-terminal helix and the N-terminal segment.

As stated above, the NMR data are consistent with MIP-2 forming a dimer in solution. The dimer interface is principally stabilized by an antiparallel β-sheet with two hydrogen bonds between strand 1 from one monomer and strand 1′ of the other monomer. There is another stabilizing

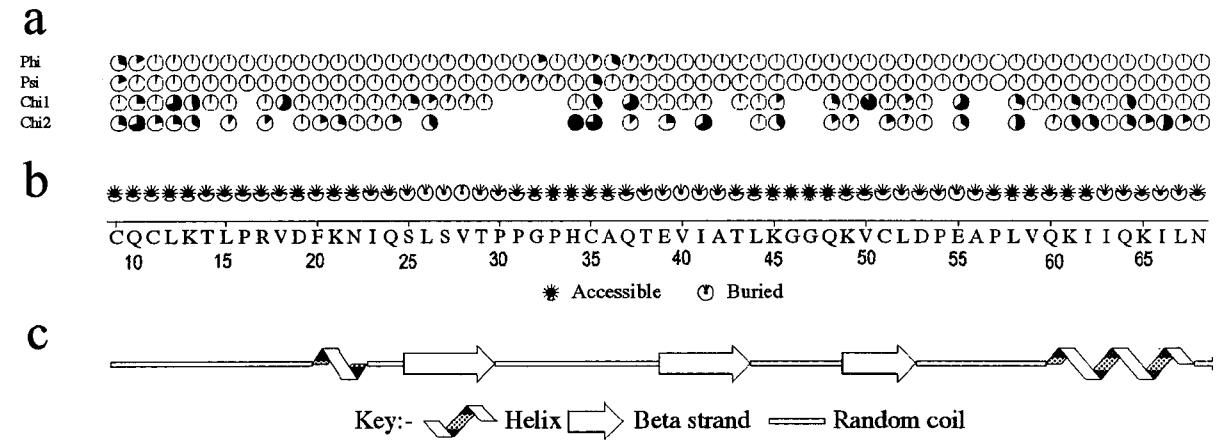

FIGURE 5: A summary of the ensemble geometry for residues 9−69 of MIP-2 as defined by PROCHECK. (a) Circular variances for the dihedral angle distributions ϕ, ψ, χ_1 and χ_2, and combinations $\phi-\psi$ and χ_1-χ_2. The larger the black area on the dial the greater the spread. (b) Solvent accessibility of each residue in MIP-2. The dark regions correspond to surface residues, while the lighter ones represent buried residues. (c) Schematic of the secondary structure of MIP-2, averaged across all the members of the ensemble.

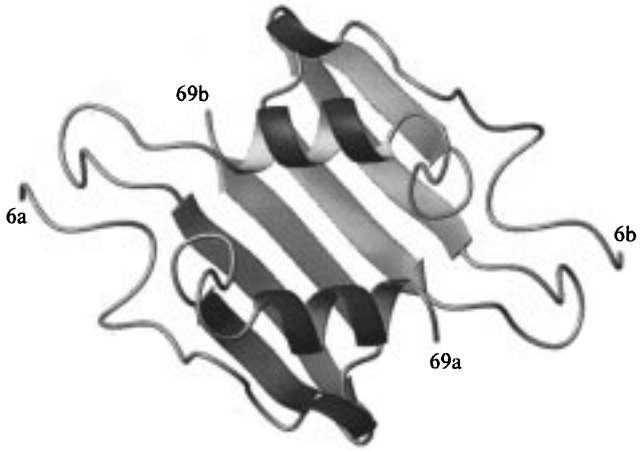

FIGURE 6: Ribbon diagram of the averaged minimized structure of the MIP-2 dimer.

interaction between the two helices involving the side-chain amide of Gln-60 of one monomer and the side-chain amide of Asn-68 of the other monomer, which serves to maintain the orientation of the C-terminal helices. There are also hydrophobic interactions between β-strand 1 of the two monomers, such as the interaction between the methylene group of Ser-25 from one monomer with the γ-methyl group of Thr-29 from the other monomer.

Comparison of the MIP-2 Structure with Other Chemokines. The solution structure MIP-2 is generally similar to the previously characterized structures of the homologous α-chemokines IL-8 (*25*, *26*) and MGSA (*27*−*29*). As noted above, however, the C-terminal α-helix of MIP-2 ends at residue 67, rather than continuing to residue 69 as in MGSA or the C-terminal residue 73 as in IL-8. A comparison of the backbone atomic rms deviations between the mean structure of MIP-2 and the solution structure of MGSA [Note that we have used the MGSA structure described by Fairbrother and co-workers (PDB accession code 1MGS (*28*)) for this comparison], the solution and X-ray structure of IL-8, and the X-ray structure of NAP-2 is given in Table 2. MIP-2 and MGSA show a rms deviation between monomers of 1.11 Å for the backbone atoms of residues 9−68, while the fits of MIP-2 to the structures of NAP-2 and the NMR and X-ray structures of IL-8 are 1.02, 1.27, and 1.19 Å, respectively. (Note that, for IL-8, residues 7−14 and 16−67 were used. Residue 15 was omitted from the superposition due to the single amino acid insertion in IL-8; for NAP-2, residues 25−84 were used.) A comparison of MIP-2 with the MGSA, NAP-2, and IL-8 (NMR and X-ray) structures shows that the β-sheet backbone rms deviation values were 0.40 Å, 0.41, 0.45, and 0.36 Å respectively. When the C-terminal α-helix is included, the rms deviation between MIP-2 and the MSGA, NAP-2, and IL-8 (NMR and X-ray) structures increases to 0.74, 0.53, 0.57, and 0.52 Å respectively, which suggests that the packing of the helix onto the sheet is different among the three proteins. Inclusion of the loop residues 53−59 significantly increases the rms deviation values between MIP-2 and the MSGA, NAP-2, and IL-8 (NMR and X-ray) structures to 1.10, 0.91, 1.02, and 0.93 Å, respectively. Inclusion of the loop residues 30−38 and the N-terminal residues 9−24 results in more modest increases in the rms deviation values, while inclusion of the residues making up the 40s loop has little impact on the rms deviation values.

Generally, rms deviation values made at the dimer level are larger than those made at the monomer level. Analysis of the structures with the program PROMOTIF (*71*) indicates that much of this increase arises from differences in positioning of the helix on top of the β-sheet. In MIP-2, the distance of closest approach for the helices is 13.4 Å, which is exactly midway between the distance observed in the IL-8 X-ray structure (11.7 Å) and the distance observed in the IL-8 NMR structure (15.1 Å). In the MGSA structure, this distance is 11.4 Å, whereas it is 10.7 Å in the NAP-2 structure. In addition, the helix interaxial angle in MIP-2 is 145° whereas this angle is 172° in the NMR structures of IL-8 and MGSA, 164° in the X-ray structure of IL-8, and 154° in NAP-2. The dimeric structure of MIP-2 appears to most closely resemble one of the dimers of PF-4; in this protein, the analogous helices have an interhelical distance of 13.7 Å and an interaxial angle of 154°. The structural basis for these differences in quaternary structure is still unclear (see ref *39* for discussion), but it is unlikely that they play a major role in determining receptor specificity since the monomeric forms of several CXC chemokines have been shown to be fully functional (*40*, *72*).

Table 2: Superpositions of MIP-2, MGSA, IL-8, and NAP-2 Monomers (Dimers)

residues[c]	rmsd (Å)[a] of MIP-2[b] vs MIP-2 (backbone)	MIP-2 (heavy atoms)	MGSA[d] (backbone)	IL-8(NMR)[e] (backbone)	IL-8(X-ray)[f] (backbone)	NAP-2[g] (backbone)
β-sheet (25−29, 39−44, 48−52)	0.15 ± 0.03	0.54 ± 0.06	0.40	0.45	0.36	0.41
β-sheet + α-helix (25−29, 39−44, 48−52, 60−68)	0.21 ± 0.05	0.66 ± 0.06	0.74	0.57	0.52	0.53
β-sheet + α-helix + 50s (25−29, 39−44, 48−68)	0.22 ± 0.05	0.68 ± 0.06	1.10	1.02	0.93	0.91
β-sheet + α-helix + 50s + 40s (25−29, 39−68)	0.22 ± 0.05	0.70 ± 0.05	1.07	1.00	0.92	0.90
β-sheet + α-helix + 50s + 40s + 30s (25−68)	0.44 ± 0.12	0.81 ± 0.08	1.12	1.13	1.02	0.99
β-sheet + α-helix + 50s + 40s + 30s + N-term (9−68)	0.49 ± 0.13	0.90 ± 0.10	1.11(1.28)	1.27(1.55)	1.19(1.36)	1.02(1.10)

[a] The RMSDs are calculated from a best fit superposition between residues 9 and 68 of MIP-2 and the corresponding residues of MGSA (9−68), IL-8 (7−14 and 16−67), or NAP-2 (25−84). Comparisons at the monomer level are listed first followed by comparisons at the dimer level (in parentheses). [b] Average structure of 20 structures. [c] Residues numbered according to MIP-2 sequence. [d] PDB accession code 1mgs. [e] PDB accession code 1il8. [f] PDB accession code 3il8. [g] PDB accession code 1nap.

The superposition of the MIP-2 monomer solution structure with the MGSA, IL-8 (NMR and X-ray), and NAP-2 structures is presented in Figure 7. The backbone deviations following such an overlay identify significant differences between these structures for the N-loop (which includes the ELR and CXC motifs and the turn at residues 15−19), the 30s loop, the 50s loop, and the C-terminal α-helix. Like MGSA, the ELR motif is more restrained in MIP-2 than in IL-8 as supported by NOEs between sequential amide protons involving residues 6−9; the corresponding residues in IL-8 do not have sequential d_{NN} NOEs (*73*). Significant differences are observed for other N-loop residues: Val-18 of MIP-2 is replaced by the bulkier Ile in MGSA and NAP-2 and by Phe in IL-8; Asp-19 of MIP-2 is replaced by the bulkier His in MGSA, IL-8, and NAP-2. In addition, the size of the 15−19 loop is smaller (one residue shorter) in MIP-2 as compared with IL-8. The net result of these changes is different steric packing between this peptide segment and the sheet and the helix, and a pronounced kink at residues 18 and 19 in the N-loop of MIP-2.

Residue Cys-9 in the CXC motif of the N-loop is linked to the 30s loop (residues 30−38, MIP-2 numbering) via a disulfide bond. Inspection of Table 2 and Figure 7 reveals that the orientation of the 30s loop in MIP-2 is most similar to the orientation seen in MGSA. The orientation of this loop in IL-8, particularly in the IL-8 NMR structure, is most dissimilar to the MIP-2 structure. The change in the conformation of the N-loop resulting from the different packing arrangement of residues 18−19 in MIP-2 may be at least partially responsible for the different orientation of the 30s loop in MIP-2 versus IL-8. It is also interesting to note that in the NMR and X-ray structures of IL-8, hydrogen bonds are observed between His-33 (IL-8 numbering) and either Gln-8 (NMR) or Glu-29 (X-ray), which are absent in MIP-2, MGSA, and NAP-2. On the other hand, the interaction between the amide proton of Gln-8 (Gln-10 in MIP-2) and the buried side chain of Glu-38 (Glu-39 in MIP-2) that is observed in the NMR and X-ray structures of IL-8 is preserved in MIP-2. This interaction, which is also seen in the structures of MGSA and NAP-2, has been shown to be responsible for the large downfield chemical shift of the amide proton of this glutamine residue that is observed in CXC chemokines that have been examined to date by NMR, including MIP-2 (*74*).

The change in the conformation of the N-loop may also have an impact on the orientation of the 50s loop. While Cys-11 in the CXC motif is not linked directly to the 50s loop, it does form a disulfide bond with Cys-51 immediately adjacent to this loop. In addition, there are several nonconservative changes in the amino acid sequences of the 50s loop among the various chemokines that likely contribute to the different orientations of the 50s loop that can be seen in Figure 7.

Structure and Function. It has been shown that IL-8 and GCP-2 bring about chemotaxis and activation of neutrophils through high-affinity binding to at least two distinct receptors, CXCR-1 and CXCR-2 (*15*−*17*). MIP-2 also induces chemotaxis in human neutrophils. In contrast to IL-8, MIP-2 binds with high affinity to CXCR-2, but with low affinity to CXCR-1 (*18*). This observation is similar to results of binding studies with MGSA, NAP-2, and ENA-78. Structure−activity studies of these chemokines have been used to define regions responsible for biological activity. Results from these studies indicate that the monomer is sufficient and the ELR motif is essential for receptor binding and activation (*75*−*78*). A mutant of MIP-2 in which the first four residues were deleted was shown to exhibit high-affinity binding to the murine homologue of the IL-8 receptor, yet required a 10-fold increase in concentration relative to wild-type MIP-2 to achieve a maximal chemotactic response (*18*). This observation suggested that the four deleted residues do not participate in receptor binding, but are involved in the activation of the receptor. A second mutant of MIP-2 in which Glu-6 and Arg-8 were each mutated to alanine bound to the receptor weakly, if at all, and demonstrated that the murine receptor also requires the ELR motif for receptor binding and activation. In IL-8, this region has been shown to be flexible by ^{15}N relaxation studies (*79*), and it is disordered in the solution structure. The disorder of the ELR region in MIP-2 is not as great as IL-8 in part due to the presence of NOE correlations between Arg-8 and His-34. Thus, the orientation of the flexible 30s loop may have a role in the presentation of the ELR motif to the receptor. This may also be the case for the more structurally heterogeneous 50s loop, although a clear demonstration of this hypothesis awaits further analysis.

Sequence analysis of the six chemokines that exhibit high-affinity binding to CXCR-2 identified a 600 Å^2 surface consisting of conserved residues Glu-6, Leu-7, Arg-8, Cys-9, Cys-11, Thr-14, Gly-32, Cys-35, Glu-39, Cys-51, and Pro-54 which may form part of the receptor-binding site (*18*). Another area of high sequence homology consists of residues Lys-21 and Lys-65 which, together with the basic residue at position 61 (which is not invariant as it is an arginine in

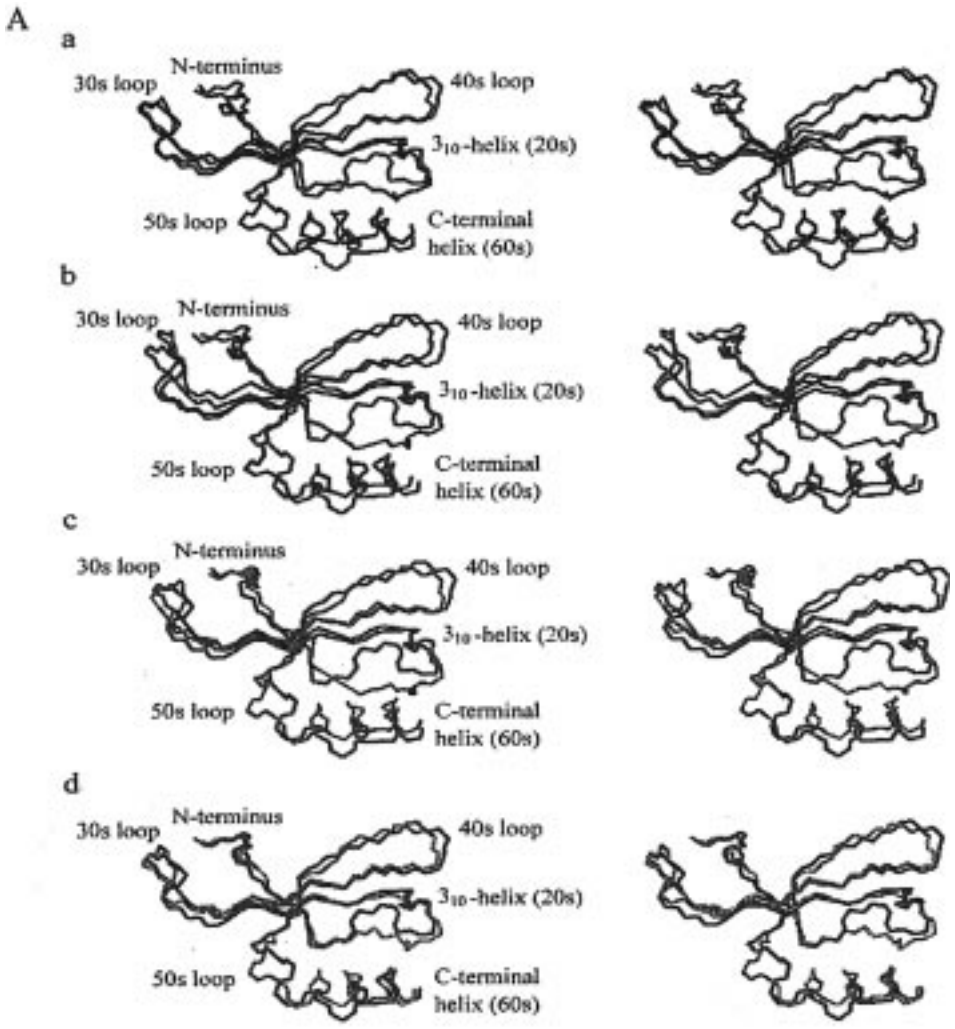

B

```
                1   5   10   15    20   25   30   35
MIP-2          AVVASELRCQCLKTLP RVDFKNIQSLSVTPPGPHCAQ
MGSA           ASVATELRCQCLQTLQ GIHPKNIQSVNVKSPGPHCAQ
NAP-2            AELRCMCIKTTS GIHPKNIQSLEVIGKGTHCNQ
muKC         GAPIANELRCQCLQTMA GIHLKNIQSLKVLPSGPHCTQ
ENA-78       AAAVLRELRCVCLQTTQ GVHPKMISNLQVFAIGPQCSK
IL-8           SAKELRCQCIKTYSKPFHPKFIKELRVIESGPHCAN
GCP-2      GPVSAVLTELRCTCLRVTL RVNPKTIGKLQVFPAGPQCSK

                40   45   50  55    60   65   70
MIP-2      TEVIATLKGGQKVCLDPEAPLVQKIIQKILNKGKAN
MGSA       TEVIATLKNGRKACLNPASPIVKKIIEKMLNSDKSN
NAP-2      VEVIATLKDGRKICLDPDAPRIKKIVQKKLAGDESAD
muKC       TEVIATLKNGREACLDPEAPLVQKIVQKMLKGVPK
ENA-78     VEVVASLKNGKEICLDPEAPFLKKVIQKILDGGNKEN
IL-8       TEIIVKLSDGRELCLDPKENWVQRVVEKFLKRAENS
GCP-2      VEVVASLKNGKQVCLDPEAPFLKKVIQKILDSGNK
```

FIGURE 7: (A) Best fit superpositions of backbone atoms of a single monomer from the mean MIP-2 coordinates (red) on the (a) MGSA (blue), (b) IL-8 (NMR) (green), (c) IL-8 (X-ray) (purple), and (d) NAP-2 (orange) structures; (B) alignment of the primary sequences of α-chemokines MIP-2, MGSA, NAP-2, muKC, ENA-78, IL-8 and GCP-2. The residue numbers of MIP-2 are shown on the top. The ELR motif is in italics, and the conserved cysteines are in bold.

IL-8 and a lysine in the other chemokines), form a highly positively charged region on the surface of the protein (Figure 8). Additional positive charges in this region in MIP-2 include Lys-45 (which is a serine in IL-8 but is conserved in the other chemokines) and Arg-17 (which is not conserved). This positively charged region may be involved in binding negatively charged moieties on the receptor. Alternatively, this region may be involved with binding the sulfate groups in heparin sulfate proteoglycans and, hence, have a role in presentation to the receptor or in the dynamics of protein binding in vivo. It is interesting to note in this regard that various chemokines may have differential selec-

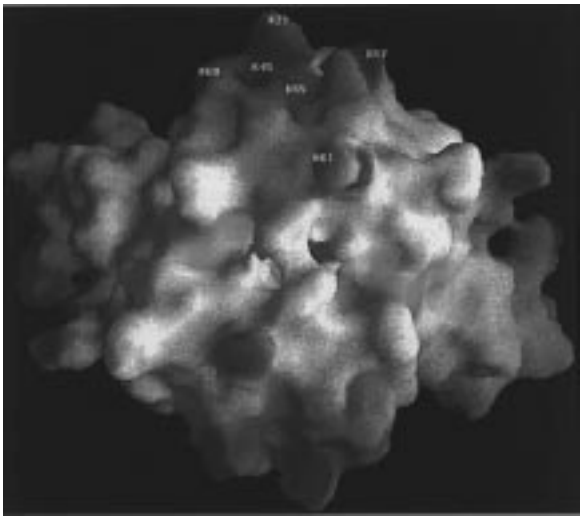

FIGURE 8: GRASP (*82*) electrostatic surface representation of the MIP-2 dimer (residues 6−69). Positively charged regions are shown in blue, and negatively charged regions are shown in red.

tivities for glycosaminoglycan families (*81*). Furthermore, IL-8, MCP-1, MIP-1α, and RANTES have been shown to oligomerize in the presence of heparin, suggesting that glycosaminoglycans may indeed have a role in raising the local concentration of chemokines or in the way chemokines interact with their receptors (*81*).

An alignment of chemokines that bind to CXCR-1 is not possible because IL-8 is the only identified chemokine with high-affinity binding to this receptor. Nonetheless, sequence differences between IL-8 and MIP-2, MGSA, KC, NAP-2, and ENA-87 must account for receptor specificity. A previous analysis identified 14 residues that have differences in charge, aromaticity, and geometric constraints (e.g., amino acids involving glycine or proline) among IL-8 and the other chemokines (*18*). One interesting observation is that seven out of these 14 residues are located between residues 13−24 (MIP-2 numbering). As described above, this is the region where significant structural differences are observed between MIP-2, MGSA, IL-8, and NAP-2. This is also in agreement with recent mutagenesis experiments to identify important residues for binding to CXCR-1 (*82*−*84*). NMR experiments involving ^{15}N-labeled IL-8 and a peptide comprising the 40 N-terminal residues of CXCR-1 identified interactions between this peptide and residues Gln-8, Thr-12, Lys-15, Phe-17, His-18, Lys-20, Phe-21, Ser-44, Gln-48, Leu-49, Cys-50, and Val-61 of IL-8 (*85*). All of this earlier work is consistent with the structural results presented here in identifying those regions of the α-chemokines that confer receptor specificity. The availability of ^{1}H and ^{15}N resonance assignments and a solution structure for MIP-2 will now allow potential interactions with the receptor and other molecules to be probed directly.

SUPPORTING INFORMATION AVAILABLE

^{1}H chemical shift assignments of MIP-2 at pH 5.25 and 303 K (5 pages) and ^{1}H-^{15}N HSQC spectrum of MIP-2 recorded at 600 MHz. Ordering information is given on any current masthead page.

REFERENCES

1. Westwick. (1991) in *Chemotactic Cyokines: Biology of the Inflammatory Peptide Supergene Family* (Lindley, I. J. D., and Kunkel, S. L., Eds.) Plenum Press, New York.
2. Kelner, G., Kennedy, J., Bacon, K., Kleyensteuber, S., Largaespada, D., Jenkins, N., Copeland, N., Bazan, J., Moore, K., and Schall, T. (1994) *Science 266*, 1395−1399.
3. Pan, Y., Lloyd, C., Zhou, H, Dolich, S., Deeds, J., Gonzalo, J. A., Vath, J., Gosselin, M., Ma, J., Dussault, B., Woolf, E., Alperin, G., Culpepper, J., Gutierriz-Ramos, J. C., and Gearing, D. (1997) *Nature 387*, 611−617.
4. Sherry, B., and Cerami, A. (1991) *Curr. Opin. Immunol. 3*, 56−60.
5. Wolpe, S., and Cerami, A. (1989) *FASEB J. 3*, 2565−2573.
6. Feng, L., Xia, Y., Yoshimura, T., and Wilson, C. B. (1995) *J. Clin. Inv. 95*, 1009−1017.
7. Kasama, T., Streiter, R., Lukacs, N., Lincoln, P., Burdick, M., and Kunkel, S. (1995) *J. Clin. Inv. 95*, 2868−2876.
8. Frevert, C. W., Farone, A., Danaee, H., Paulauskis, J. D., and Kobzik, L. (1995*) Inflammation 19*, 133−142.
9. Standiford, T. J., Strieter, R. M., Lukacs, N. W., and Kunkel, S. L. (1995) *J. Immunol. 155*, 2222−2229.
10. Calacano, C., Lee, J., Kikly, K., Pitts-Meek, S., Hulgren, B., Wood, W. I., and Moore, M. W. (1994) *Science 265*, 682−684.
11. Broxmeyer, H. E., Sherry, B., Lu, L., Cooper, S., Carow, C., Wolpe, S. D., and Cerami, A. (1989) *J. Exp. Med. 170*, 1583−1594.
12. Broxmeyer, H. E., Sherry, B., Lu, L., Cooper, S., Oh, K. O., Tekamp-Olson, P., Kwon, B. S., and Cerami, A. (1990) *Blood 76*, 1110−1116.
13. Broxmeyer, H. E., Sherry, B., Cooper, S., Ruscetti, F. W., Williams, D. E., Arosio, P., Kwon, B. S., and Cerami, A. (1991*) J. Immunol. 147*, 2586−2594.
14. Broxmeyer, H. E., Cooper, S., Cacalano, G., Hague, N., Bailish, E., and Moore, M. (1996*) J. Exp. Med. 184*, 1825−1832.
15. Holmes, W. E., Lee, J., Kuang, W. J., Rice, G. C., and Wood, W. I. (1991) *Science 253*, 1278−1280.
16. Murphy, B., and Tiffany, H. L. (1991) *Science 253*, 1280−1283.
17. Wuyts, A., Osselaer, N. V., Haelens, A., Samson, I., Herdewijn, P., Ben-Baruch, A., Oppenheim, J. J., Proost, P., and Van Damme, J. (1997) *Biochemistry 36*, 2716−2723.
18. Jerva, L. F., Sullivan, G., and Lolis, E. (1997) *Protein Sci. 6*, 1643−1652.
19. Bozic, C. R., Kolakowaski, L. F. Jr., Gerard, N. P., Garcia-Rodriguez, C., von Uexkull-Guldenband, C., Conklyn, M. J., Breslow, R., Showell, H. J., and Gerard, C. (1995) *J. Immunol. 154*, 6049−6057.
20. Moser, B., Schumacher, C., von Tscharne, V., Clark-Lewis, I., and Baggiolini, M. (1991) *J. Biol. Chem. 266*, 10666−10671.
21. Petersen, F., Flad, H., and Brandt, E. (1994) *J. Immunol. 152*, 2467−2478.
22. Bozic, C. R., Gerard, N. P., and Gerard, C. (1996) *Am. J. Respir. Cell Mol. Biol. 14*, 302−308.
23. Zhang, X., Chen, L., Bancroft, D. P., Lai, C. K., and Maione, T. E. (1994) *Biochemistry 33*, 8361−8366.
24. St. Charles, R., Walz, D. A., and Edwards, B. F. P. (1989) *J. Biol. Chem. 264*, 2092−2099.
25. Baldwin, E. T., Weber, I. T., St. Charles, R., Xuan, J.-C., Apella, E., Yamanda, M., Matsushima, K., Edwards, B. F. P., Clore, G. M., Gronenborn, A. M., and Wlodower, A. (1991) *Proc. Natl. Acad. Sci. U.S.A.* 88, 502−506.
26. Clore, G. M., Appella, E., Yamada, M., Matsushima, K., and Gronenborn, A. (1990) *Biochemistry 24*, 1689−1696.
27. Fairbrother, W. J., Reilly, D., Colby, T. J., Hesselgesser, J., and Horuk, R. (1993*) FEBS Lett. 330*, 302−306.
28. Fairbrother, W. J., Reilly, D., Colby, T. J., Hesselgesser, J., and Horuk, R. (1994*) J. Mol. Biol. 242*, 252−270.
29. Kim, K.-S., Clark-Lewis, I., and Sykes, B. D. (1994) *J. Biol. Chem. 269*, 32909−32915.
30. Hanzawa, H., Haruyama, H., Watanabe, K., and Tsurufuji, S. (1994) *FEBS Lett. 354*, 207−212.

31. Malkowski, M. G., Wu, J. Y., Lazar, J. B., Johnson, P. H., and Edwards, B. F. (1995) *J. Biol. Chem. 270*, 7077−7087.
32. Lodi, P., Garrett, D., Kuszewski, J., Tsang, M., Weatherbeen, J., Leonard, W., Gronenborn, A., and Clore, G. (1994) *Science 263*, 1762−1767.
33. Skelton, N. J., Aspiras, F., Ogez, J., and Schall, T. J. (1995) *Biochemistry 34*, 5329−5342.
34. Chung, C., Cooke, R. M., Proudfoot, A. E. I., and Wells, T. N. C. (1995) *Biochemistry 34*, 9307−9314.
35. Lubkowski, J., Bujacz, G., Boque, L., Domaille, P. J., Handel, T. M., and Wlodawer, A. (1997) *Nat. Struct. Biol. 4*, 64−69.
36. Kim, K.-S., Rajarathnam, K., Clark-Lewis, I., Sykes, B. D. (1996) *FEBS Lett. 395*, 277−282.
37. Meunier, S., Bernassau, J. M., Guillemot, J. C., Ferrara, P., and Darbon, H. (1997) *Biochemistry 36*, 4412−4422.
38. Dealwis, C., Fernandez, E. J., Thompson, D. A., Simon, T. J., Siani, M. A., and Lolis, E. (1998) *Proc. Natl. Acad. Sci. U.S.A.* (In press).
39. Fairbrother, W. J. and Skelton, N. J. (1996) in *Chemoattractant Ligands and Their Receptors* (Horuk, R., Ed.) pp 55−86, CRC Press, New York.
40. Rajarathnam, K., Sykes, B. D., Kay, C. M., Dewald, B., Geiser, T., Baggiolini, M., and Clark-Lewis, I. (1994) *Science 264*, 90−92.
41. Braunschweiler, L., Bodenhausen, G., and Ernst, R. R. (1983) *Mol. Phys. 48*, 535−560.
42. Bax, A., and Davis, D. G. (1985) *J. Magn. Reson. 65*, 355−360.
43. Griesinger, C., Otting, G., Wuthrich, K., and Ernst, R. R. (1988) *J. Am. Chem. Soc. 110*, 7870−7873.
44. Kumar, A., Ernst, R. R., and Wuthrich, K. (1980) *Biochem. Biophys. Res. Commun. 95*, 1−6.
45. Bodenhausen, G., Kogler, H., and Ernst, R. R. (1984) *J. Magn. Reson. 58*, 370−388.
46. Bothner-By, A. A., Stephens, R. L., Lee, J. T., Warren, C. D., and Teanloz, R. W. (1984*) J. Am. Chem. Soc. 106*, 811−813.
47. Rance, M., Sorensen, O. W., Bodenhausen, G., Wagner, G., Ernst, R. R., and Wuthrich, K. (1983) *Biochem. Biophys. Res. Commun. 117*, 479−485.
48. States, D. J., Haberkorn, R. A., and Ruben, D. J. (1982) *J. Magn. Reson. 48*, 286−292.
49. Smallcombe, S. H., Patt, S. L., and Keifer, P. A. (1995) *J. Magn. Reson., Ser. A 117*, 295−303.
50. McCoy, M. A., and Mueller, L. (1992) *J. Am. Chem. Soc. 114*, 2108−2110.
51. Bodenhausen, G., and Ruben, D. L. (1980) *Chem. Phys. Lett. 69*, 185−188.
52. Wuthrich, K. (1986) *NMR of Proteins and Nucleic Acids*, John Wiley & Sons, Inc., New York.
53. Tropp, J. (1980) *J. Chem. Phys. 72*, 6035−6043.
54. Koning, T. M. G., Boelens, R., and Kaptein, R. (1990) *J. Magn. Reson. 90*, 111−123.
55. Zuiderweg, E. R. P., Boelens, R., and Kaptein, R. (1985) *Biopolymers 24*, 601−610.
56. Wagner, G., Braun, W., Havel, T. F., Schaumann, T., Go, N., and Wuthrich, K. (1987) *J. Mol. Biol. 196*, 611−639.
57. Basu, V. J. (1989) *Methods Enzymol. 177*, 132−149.
58. Nilges, M. (1993) *Proteins: Struct., Funct., Genet. 17*, 297−309.
59. Nilges, M. (1995) *J. Mol. Biol. 245*, 645−660.
60. Fletcher, C. M., Jones, D. N. M., Diamond, R., and Neuhaus, D. (1996) *J. Biomol. NMR 8*, 292−310.
61. Kim, Y., and Prestegard, J. H. (1989*) J. Magn. Reson. 84*, 9−13.
62. Clubb, R., T., Fergusen, S. B., Walsh, C. T., and Wagner, G. (1994) *Biochemistry 33*, 2761−2772.
63. Stein, E. G., Rice, L. M., and Brunger, A. T. (1997) *J. Magn. Reson. 124*, 154−164.
64. Brunger, A. T. (1992) *X-PLOR, Version 3.1. A System for X-ray Crystallography and NMR*, Yale University Press, New Haven.
65. Laskowski, R. A., MacArthur, M. W., Moss, D. S., and Thornton, J. M. (1993) *J. Appl. Crystallogr. 26*, 283−291.
66. Wishart, D. S., Sykes, B. D., and Richards, F. M. (1992) *Biochemistry 31*, 1647−1651.
67. Kraulis, P. J., Clore, G. M., Nilges, M., Jones, T. A., Petterson, G., Knowles, J., and Gronenborn, A. M. (1989) *Biochemistry 28*, 7241−7257.
68. Ramachandran, G. N., Ramakrishnan, C., and Sasisekharan, V. (1963) *J. Mol. Biol. 7*, 95−99.
69. Allen, F. H., and Johnson, O. (1991) *Acta Crystallogr., Sect. B 47*, 62−67.
70. MacArthur, M. W., and Thornton, J. M. (1993) *Proteins 17*, 232−251.
71. Hutchinson, E. G., and Thornton, J. M. (1996) *Protein Sci. 5*, 212−220.
72. Rajarathnam, K., Kay, C. M., Dewald, B., Wolf, M., Baggiolini, M., Clark-Lewis, I., and Sykes, B. D. (1997) *J. Biol. Chem. 272*, 1725−1729.
73. Clore, G. M., Appella, E., Yamada, M., Matsushima, K., and Gronenborn, A. (1989) *J. Biol. Chem. 264*, 18907−18911.
74. Rajarathnam, K., Clark-Lewis, I., Dewald, B., Baggiolini, M., and Sykes, B. D. (1996) *FEBS Lett. 399*, 43−46.
75. Clark-Lewis, I., Dewald, B., Loetscher, M., and Moser, B. (1994) *J. Biol. Chem. 269*, 16075−16081.
76. Clark-Lewis, I., Schumacher, C., Baggiolini, M., and Moser, B. (1991) *J. Biol. Chem. 266*, 23128−23134.
77. Clark-Lewis, I. A., Dewald, B., Geiser, T., Moser, B., and Baggiolini, M. (1993) *Proc. Natl. Acad. Sci. U.S.A. 90*, 3574−3577.
78. Hebert, C. A., Vitangcol, R. V., and Baker, J. B. (1991) *J. Biol. Chem. 266*, 18989−18994.
79. Grasberger, B. L., Gronenborn, A. M., and Clore, G. M. (1993) *J. Mol. Biol. 230*, 364−372.
80. Nicholls, A., Sharp, K. A., and Honig, B. (1991) *Proteins 11*, 281−296.
81. Hoogewerf, A. J., Kuschert, G. S. V., Proudfoot, A. E. I., Borlat, F., Clark-Lewis, I., Power, C. A., and Wells, T. N. C. (1997) *Biochemistry 36*, 13570−13578.
82. Scraufstatter, I. U., Ma, M., Oades, Z. G., Barritt, D. S., and Cochrane, C. G. (1995) *J. Biol. Chem. 270*, 10428−10431.
83. Hammond, M. E. W., Shymala, V., Siani, M. A., Gallegos, C. A., Feucht, P. H., Abbott, J., Lapointe, G. R., Moghadam, M., Khoja, J., Zakel, J., and Tekamp-Olson, P. (1996) *J. Biol. Chem. 271*, 8228−8235.
84. Lowman, H. B., Slagle, P. H., DeForge, L. E., Wirth, C. M., Gillece-Castro, B. L., Bourell, J. H., and Fairbrother, W. J. (1996) *J. Biol. Chem. 271*, 14344−14352.
85. Clubb, R. T., Omichinski, J. G., Clore, G. M., and Gronenborn, A. M. (1994) *FEBS Lett. 338*, 93−97.

BI980112R